Spectrochimica Acta Part B: Atomic Spectroscopy 210 (2023) 106809

Contents lists available at ScienceDirect

Spectrochimica Acta Part B: Atomic Spectroscopy

journal homepage: www.elsevier.com/locate/sab

Angle Resolved-XRF analysis of Puebla ceramic decorations

Jacopo Orsilli *, Marco Martini, Anna Galli

Università degli Studi di Milano-Bicocca, Dipartimento di Scienza dei Materiali, via Roberto Cozzi 55, Milano 20125, Italy

ARTICLE INFO

Keywords:
X-ray fluorescence
Angle-Resolved X-ray fluorescence
Cultural heritage
Ceramic
Layered samples
Archaeology

ABSTRACT

With Angle Resolved XRF (AR-XRF) the sample is investigated at different angles of detection and irradiation. The geometry of analysis indeed affects the intensity of the characteristic elemental fluorescence signal of the sample, which depends on the element distribution inside the sample. This technique has already proved to be very useful in analyzing metallic bilayer samples. In this paper, we applied AR-XRF to study a real case in the field of Cultural Heritage, with the analysis of a glazed ceramic coming from Puebla, Mexico. The analysis of the decorations, which present different thicknesses and compositions, has shown the limits of the technique, especially in the case of thick and diffused layers, and the importance of a priori knowledge to retrieve structural information in the case of a complex system with a great number of variables.

1. Introduction

X-ray fluorescence (XRF) is a technique commonly employed for the characterization of Cultural Heritage artifacts due to its capability to retrieve the elemental composition of a sample with relatively fast non-invasive measurements. Moreover, the development of portable and hand-held instrumentation has allowed for performing in-situ measurements (like in a museum, a private collection, or the original archeological site). The possibility to detect a wide range of elements [1] (from aluminum to uranium) using hand-held spectrometers, allows the analysis of a wide range of materials, such as ceramics, metals, and glass, among others… The greatest advantage of XRF is the possibility, under certain conditions, to perform non-invasive quantitative analyses (i.e., avoiding any pretreatment or sub-sampling of the specimen). As a rule, samples must be flat and homogenous, which are characteristics seldom found in Cultural Heritage artifacts. Indeed, historical, and archeological artifacts are, most of the time, inhomogeneous samples, not only because they can be made of different materials (like ceramics or pigments), but also because they can exhibit layers that are considered 'intermediate' thickness for the investigated x-ray energies. These layers may originate from the manufacturing of the sample, such as glazes covering a ceramic object, or the gilding of a metal; but also, be the result of changes in surface composition caused by aging and other alteration processes [2–12]. Additionally, these objects are usually unique, rare, or exceptionally valuable, hence, the use of non-invasive and portable techniques may be mandatory [13–23]. That's why the development of new approaches for non-invasive techniques is now on the agenda of many research groups, extending the range and reliability of the acquired dataset [24,25].

Many methods can be employed non-invasively for the analysis of layered samples; the best results can be achieved with IBA techniques, like Rutherford Backscattering Spectroscopy (RBS), usually coupled with Particle Induced X-ray Emission (PIXE). RBS allows the characterization of the layered structure of a sample by evaluating the energy distribution of the backscattered particles, which depends on the mass of the hit nucleus, the scattering angle, and the thickness of each layer [26–30]. The volume of the interaction of the incident particles is limited to the surface of the sample and depends on the particles' energy. Irradiation using different particle energies (the so-called "differential PIXE" [31–34]) can be applied to discriminate among the different contributions of layers in the sample. The drawback of these techniques is the need to access a particle accelerator, which is not always possible for many laboratories. That's why different methods have been proposed for the analysis of layered samples using X-ray fluorescence, such as the measurement of K_α/K_β or L_α/L_β intensities ratio [35–38], often applied for the analysis of metal artifacts; or the use of Monte-Carlo simulations [39–42]. Otherwise, it's possible to place polycapillary lenses in front of the source and the detector to perform confocal-XRF and obtain a 3D scan of the artifact [43–50], with a spatial resolution down to a few tens of micrometers. Finally, nanometer's scale layers can be analyzed through Grazing Emission-XRF (GE-XRF), Grazing Incident-XRF (GI-XRF), or X-Ray Reflectivity (XRR) using well-collimated synchrotron beams. These last techniques exploit reflection and refraction phenomena and the production of standing-wave fields [51–53].

* Corresponding author.
E-mail address: jacopo.orsilli@unimib.it (J. Orsilli).

https://doi.org/10.1016/j.sab.2023.106809
Received 22 June 2023; Received in revised form 16 October 2023; Accepted 17 October 2023
Available online 18 October 2023

Fig. 1. A) Puebla ceramic sample (*courteously supplied by Gabinete de Arqueología, Havana, Cuba*). The white glaze is characterized by the presence of tin and lead. The blue decoration by the presence of cobalt and the black decorations by the high amount of iron. Below, are images collected from the fractures to observe the different layers with the microscope, in image B) the blue glaze can be observed, and in image C) the black spot and black stripe. (For interpretation of the references to color in this figure legend, the reader is referred to the web version of this article.)

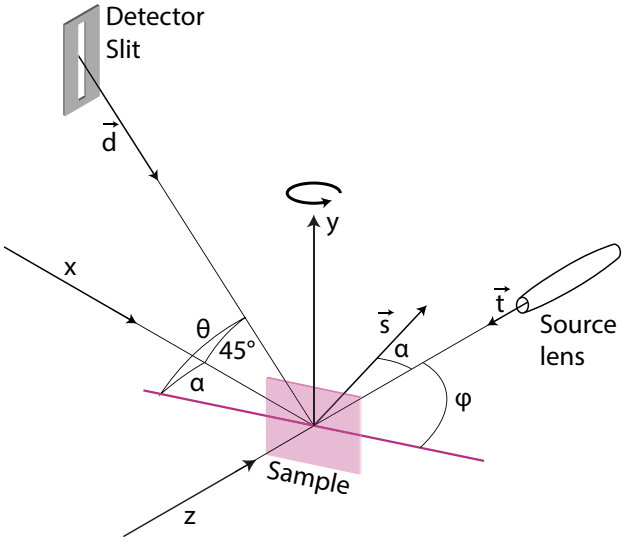

Fig. 2. Geometry of the multipurpose XRF spectrometer, the sample can be moved along axes x, y, and z and tilted around the y-axis; it is also shown the slit in front of the detector. From [57].

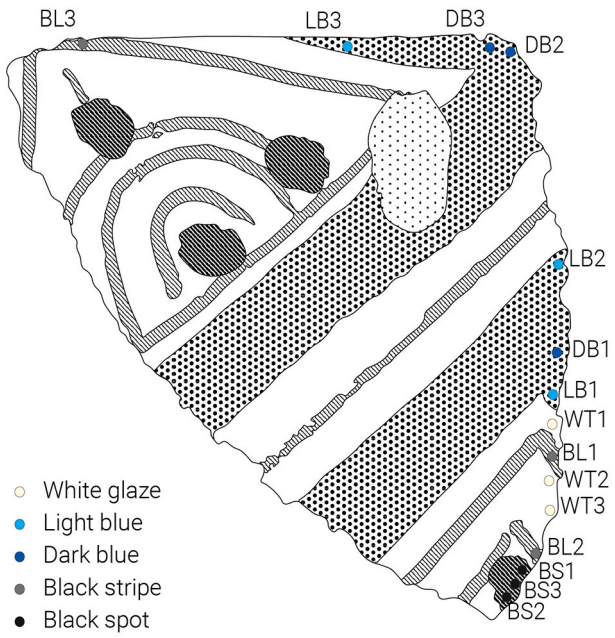

Fig. 3. Map of the points where spectra were collected with AR-XRF; the color of the spots represents the color of the glaze.

Another technique that exploits angular scanning is Angle Resolved-XRF [54–56]. This method was proposed in 2001 by Fiorini et al. [50]. Differently from the GE-XRF technique, the angle of detection here is not limited to a small range around the critical angle, but to a broader range, from 0° to 90°.

In our previous work [57], we evaluated the capability of AR-XRF to analyze, distinguish, and characterize different laboratory-made gilded samples. In the investigation reported in this paper, we take a step further, employing AR-XRF to analyze the decoration of a Majolica ceramic sherd, evaluating the structure, composition, and thickness of the different decorations found on its surface. For the study, the ceramic samples investigated have three important characteristics that will be exploited in the data analysis: (I) the ceramic body and the white glaze compositions are known [58] and their thickness can be considered infinite; (II) there is an element common in both layers that can be employed as a reference; (III) the colored glaze contains in great amount characteristic elements that are not present (or are present in low amount) in the layer below. We will finally evaluate what are the potential applications and the limits of this technique, especially when dealing with this kind of sample.

2. Theory

XRF is a well-known non-invasive technique in which an X-ray source impinges on a surface, exciting its atoms. If the energy is high enough the atom is ionized through photoelectric absorption, causing a relaxation process that emits a characteristic electromagnetic radiation in the form of x-rays. The attenuation of X-rays, and their absorption through a given layer, depends on the layer composition and density following the Lambert-Beer law:

$$I(E) = I_0(E)exp\left[-\frac{\mu(E)\rho x}{sin\alpha}\right] \quad (1)$$

where I_0, I are the source and attenuated intensities at the energy E, μ is the massive attenuation coefficient of the layer, ρ is its density, x is the sample thickness, and α is the angle of incidence. XRF can then be described as a bulk technique, as the results obtained depend on the whole volume of interaction, which in turn depends on the energy of the

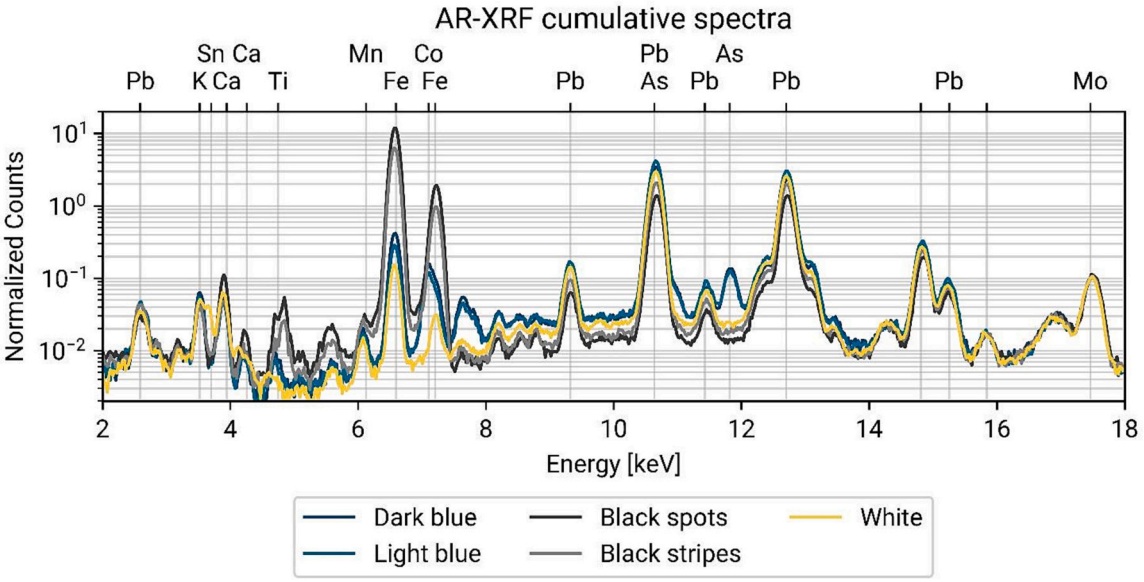

Fig. 4. Cumulative spectra of the decorations, each color represents one decoration; the top legend highlights the element lines, and the bottom axis is the energy. The spectra are rescaled by normalization to the Rayleigh scattering peak for representation purposes and are shown on a logarithmic scale.

X-rays and the composition of the layer. Eq. 1 also relates the probed depth with the radiation energy; thus, we can define two different depths of interaction: the 'penetration depth' is the depth reached by the energies of the source radiation and defines the volume of the interaction of the different energies of the source with the sample, the 'escape depth' is the maximum depth from which the fluorescence radiation of an element can be detected. The depth investigated by an XRF measurement, for each fluorescence energy, is the minimum of these two values.

The equation that relates the measured fluorescence signal to the experimental conditions and the sample properties is Sherman's equation (Eq. 2) [59], which for layered samples, and disregarding enhancement phenomena, has this form:

$$I_{m,q} = G_q P_{q,l}\, w_{m,q} \int_{S_q}^{E_M} I_0(E)\tau_q(E)\frac{1-exp\left[-\rho_m h_m \mu_m^*(E,E_q,\phi,\theta)\right]}{\mu_m^*(E,E_q,\phi,\theta)} exp\left[-\sum_{j=1}^{m-1}\rho_j h_j \mu_j^*(E,E_q,\phi,\theta)\right] dE \quad (2)$$

where $I_{m,q}$ is the fluorescence intensity of the element q in layer m, $P_{q,l}$ is the probability of x-ray production for a given fluorescence line, $w_{q,m}$ is the concentration of the element q in layer m, S_q is the energy of the photoelectric absorption edge for the given group of lines of element q, E_M is the maximum energy of the source, $\tau_q(E)$ is the photoelectric absorption cross-section of the element q, ρ_m is the m-layer density, h_m its thickness and G is a factor accounting for the effective solid angles of excitation and measurement (the geometrical factor):

$$G_q = \frac{\Delta\Omega}{4\pi}\frac{\eta(E_q)}{sin\phi} \quad (3)$$

with $\Delta\Omega$ solid angle of the detector, ϕ angle of excitation and η efficiency of the detector. $\mu_m^*(E,E_q,\phi,\theta)$ is the effective total attenuation of the layer for the source and fluorescence energy:

$$\mu_m^*(E,E_q,\phi,\theta) = \frac{\mu_m(E)}{sin\phi} + \frac{\mu_m(E_q)}{sin\theta} \quad (4)$$

where θ is the angle of detection.

The first term containing the exponential in the numerator of the quotient considers the attenuation of both the excitation beam (with energies E) and the emitted fluorescence of element q in layer m (with energy E_q), whereas the second term with the exponential including the sum over all other layers on top of layer m considers the attenuation through the series of layers existing between layer m and the surface of the object.

Attenuation is influenced by the angle of irradiation ϕ and the angle of detection θ, as, for the Lamber-Beer law (Eq. 1), they impact the penetration and escape volumes. If a layered sample is investigated with a shallow angle of irradiation, the crossed path length inside the surface layer is increased, so that a high percentage of the source radiation is attenuated in this layer, and fewer photons can reach and excite the underlying layers or the bulk. By increasing the irradiation angle the crossed path inside the surface layers is reduced and more photons excite the bulk. Regarding the detection angle, if the sample is investigated with a shallow angle of detection, the path length crossed by the fluorescence signal emitted by the bulk is increased, thus the surface layer highly attenuates it. Thus, in general, analyses with a shallow angle of irradiation and detection enhance the signal coming from the surface, while steeper angles enhance the signal coming from the bulk. Changing the geometry of measurement can then be employed to collect the information coming from the different layers composing the sample. The analysis performed by changing the excitation and/or detection angles is called Angle-Resolved XRF (AR-XRF).

AR-XRF is based on the collection of XRF spectra at different irradiation and/or detection angles. To perform this technique, we can choose to tilt the source, the detector, or the sample around the focal point: in the latter case both the angles of irradiation and detection change. The detector and/or the source must be well collimated to ensure a small divergence in the excitation and detection angles, thus ensuring that the signal collected comes only from a limited volume of the sample at given angles.

The intensity of each element plotted versus the angle of detection/irradiation can give a hint about its distribution inside the sample.

3. Materials and methods

3.1. Sample

Majolica is a distinctively Hispanic category of glazed, wheel-thrown ceramics, distinguished by its soft earthenware paste covered by an opaque vitreous enamel or glaze. The addition of tin oxide to the glaze

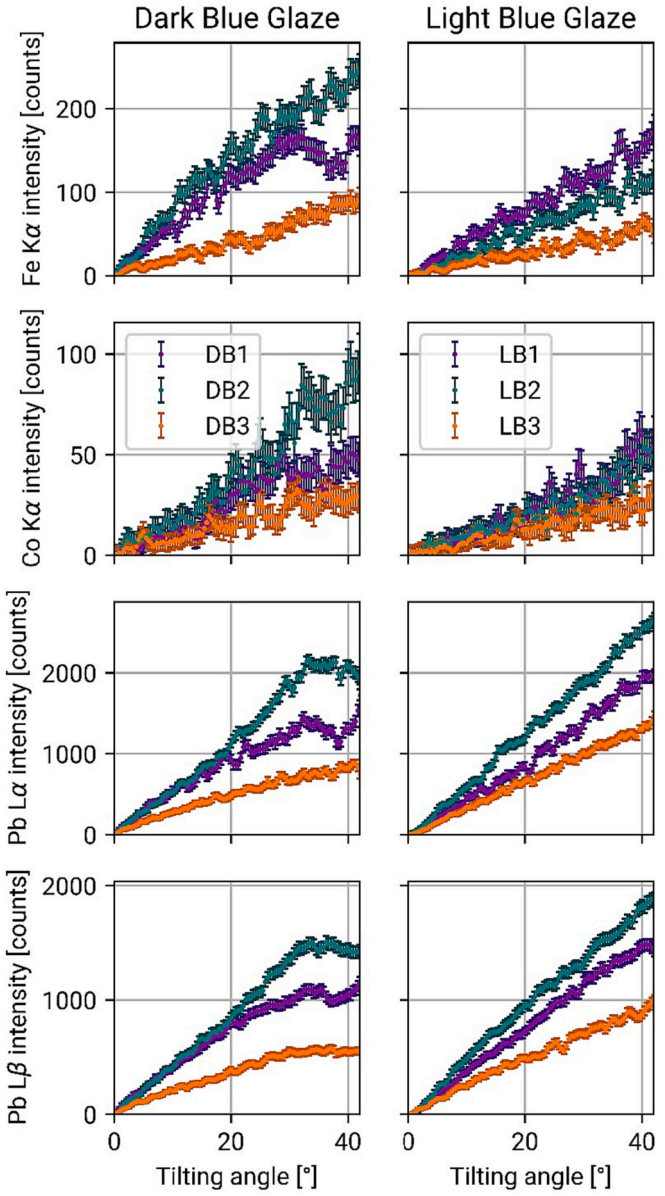

Fig. 5. Intensity profiles of the blue decorations of Fe K_{α}, Co K_{α}, Pb $L_{\alpha,}$ and Pb L_{β}. (For interpretation of the references to color in this figure legend, the reader is referred to the web version of this article.)

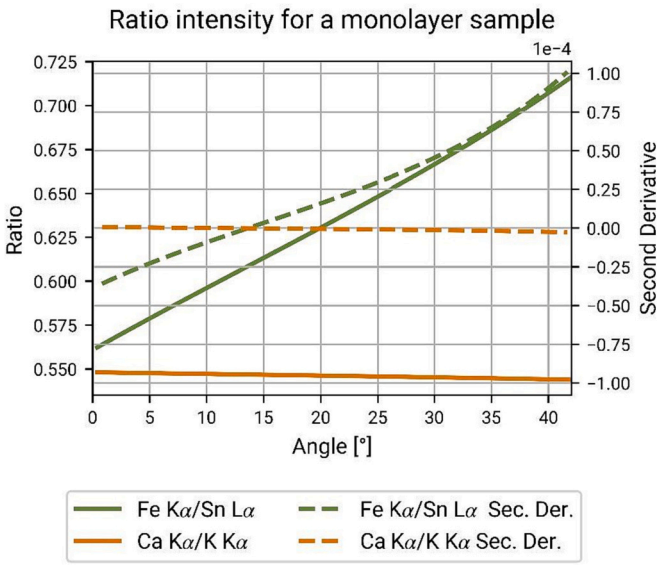

Fig. 6. Fe K_{α}/Pb L_{α} ratio for a bulk layer with a composition similar to the one of the white glaze; the solid line is the ratio (y-axis on the left), dashed lines are the second derivatives (y-axis on the right).

produces opacity, which is found also in the technically related French faience and English and Dutch delftware [58,60].

The main characteristic of Majolica is indeed the white alkali glaze that covers homogeneously the ceramic biscuit. To obtain this homogeneous white opaque glaze, artisans employed minerals of lead and tin. Lead has been added to the glaze recipe since the Roman period, as it works as a softener, allowing to heat at lower temperatures the artifact during the decoration process; instead, the addition of tin in the mixture works as an opacifier. Tin reacts with the silica mixture to create small crystals of cassiterite (SnO_2); these crystals together with the presence of quartz, feldspars, and air bubbles, scatter and reflect the light, creating the characteristic white opacity [60].

As the ingredients vary with the place of production and the availability of the raw materials, different recipes were followed around the world. In general, it was quite common to use a ratio of 1:6 lbs. of tin and lead to prepare the ground mixture, to which different substances were added. In Italy, it was common to add sand, potash, and salt; while in Spain potash was substituted with wine lees, and in Mexico potash was substituted with soda ash.

The sample analyzed is a sherd with a size of nearly 7 × 5 cm (Fig. 1A) of the *Puebla Policromo* production (1650–1725) [61]. Over the white glaze that covers homogeneously the ceramic earthenware, we have blue and black decorations. The blue decoration is characterized by the presence of cobalt as a chromophore and is clearly not homogenous in thickness: in the center, where the color is more intense (Fig. 1B), the glaze is thicker than along the borders, where the color is lighter. The black decorations (Fig. 1C) can be divided into two categories, the small stripes present a vitreous luster and seem very thin, while the black spots seem thicker and present small crystals with a submetallic luster. In both kinds of black decorations, the main composing elements are iron and lead. The most common mineralogical forms that give the black color are melanotekite ($Pb_2Fe_2Si_2O_9$), hematite (Fe_2O_3), and magnetoplumbite ($PbFe_{12}O_{19}$), and their presence depends on the firing temperature. Melanotekite is stable at low temperatures (≤875 °C) and forms small facetted plate crystals and are usually covered with primary hematite, it seems true that hematite reacts with the silica-lead melt to form melanotekite. At higher temperatures (≤1022 °C) melanotekite is dissolved and only secondary hematite is found, in this case, hematite crystals are larger than the previously formed primary hematite and more faceted. Finally, at 1023 °C hematite dissolves to form magnetoplumbite, composed of micron-sized dark hexagonal platelets [60,62].

3.2. Instrumentation

AR-XRF analyses have been performed at the Nuclear Science and Instrumentation Laboratories (NSIL) of the International Atomic Energy Agency (IAEA), Seibersdorf (Austria) using their multipurpose microbeam scanning XRF spectrometer [63].

The measurements were carried out by irradiating the sample with a diffraction X-ray tube with a Mo anode (3 kW), set with a voltage of 45 kV and an intensity of 40 mA. To perform the AR-XRF profiles we rotate the sample holder of 50° (namely from −5° to 45°) with a rotation step of 0.417° (or 7.5 mrad) (a total of 121 spectra) and a dwell time of 20 s. For each sample, we performed 3 angular scans on the different glazed areas. The area illuminated by the source goes from a circle of radius 25 μm when the sample is perpendicular to the source (namely 0°) to 35.4 μm when the sample is irradiated at 45°.

The spectrometer can perform different kinds of measurement, as it

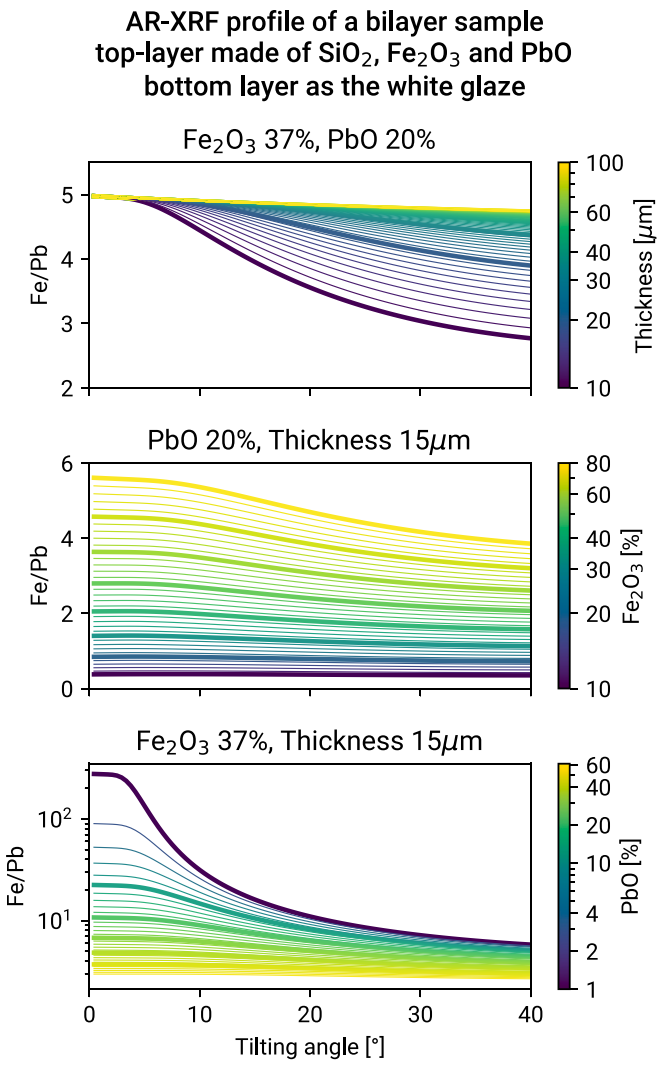

Fig. 7. Fe K_α/Pb L_α ratio for a bilayer sample where the top layer is a glaze with a variable composition of PbO, Fe_2O_3, and SiO_2, and a variable thickness, and a bulk similar to the white glaze. On top, we can observe what happens if we fix the composition with a high iron content and a low lead content, and we change the top-layer thickness; in the central plot we can observe what happens if we fix the lead concentration and the thickness, and we let vary the iron content (and the SiO_2 content which is employed as closure); in the latter plot instead we change the PbO concentration fixing thickness and iron concentration.

is equipped with two SDDs (Silicon Drift Detectors) and a movable sample-holder, so it can be employed to perform both 2D mapping and confocal-XRF experiments (3D mapping). The SDD employed has an active area of $10mm^2$, a crystal of 450 μm thickness, and an 8 μm Be window; its energy resolution is 135 eV at 5.9 keV. The amplification of the MCA allows the recording of photons until an energy of 20 keV. The detector is positioned at 45° over the *xz*-plane (Fig. 3). For AR-XRF analysis this detector was collimated with a stainless-steel vertical slit (type 1.4310) the distance between the sample and the slit is 17 mm. The slit has an opening of 60 μm and is 5 mm in height, with a thickness of 600 μm. It is placed vertically in front of the detector; thus, the mean angular resolution is 5 mrad (a minimum of 4.5 mrad at the top and a maximum of 5.6 mrad at the bottom of the slit). The effective probed volume of the sample is 25 × 85 μm. Using such a slit instead of a cylindrical collimator enhances the fluorescence signal as the radiation spread along the axis of rotation is collected. The samples are mounted on a stage that provides a 3D movement (x, y, z) and a rotation α around the vertical axis (y-axis). To ensure a better alignment of the sample in the AR-XRF analyses, we developed a sample holder that allows us to manually move the sample independently to the stage and to align its surface to the rotation axis.

As we have said previously, the decoration of the ceramic sherd can be divided into three groups, the white decorations, the blue decorations, and the black decorations. For this very reason we collected three measurement points for each kind of decoration: white glaze (WT), light blue (LB), dark blue (DB), black spots (BS), and black stripes (BL), mapped in Fig. 3. As you can see from the map, all the spots have been collected near the border of the sherd, this was a mere practical choice. As the distance between the source and the focus spot is of few millimeters, if we had analyzed areas in the center of the ceramic during the tilting of the sample, its surface would have collided with the source collimator, thus the only points we could measure are those on the borders. This problem can be resolved by increasing the source-sample distance. However, due to the mean composition of the ceramic, the distance of the measurement point from the border is higher than the escape depth, ensuring that no fluorescence signal escapes from the lateral surface of the sample, reaching the detector, where spectra at grazing angles are collected.

3.3. Data treatment

For this analysis, we followed a different strategy from the one employed in the analysis of the gilded samples [57]. The analysis of ceramic has shown the presence of many more elements; thus, we did not use the total counts in Regions of Interest (ROIs) in the XRF spectrum to retrieve the intensity profiles but we employed Pymca© [64] to fit the fluorescence peaks. In this way we could have a better estimate (although affected by the uncertainty of estimation of the interfering peak) of the peak areas of the fluorescence lines like Co K_α and Fe K_β or As K_α and Pb L_α.

Finally, due to the geometric and shadowing effect, we did not relate the profiles as they have been obtained but compared the profiles' ratio. As lead is the main element composing the white glaze in both the main layer and in the superimposed decorations, the profiles of interest have been normalized for the profile of lead L_α fluorescence line intensity. The use of intensities ratios instead of absolute values has a second advantage, as all the factors affecting homogeneously the intensity of the profile, like the source flux (but not the source shape distribution) can be neglected.

The analysis of the data has then followed these steps:

1. fitting of the XRF spectra using Pymca©,
2. correction of the angle using a surface element fluorescence profile,
3. calculation of the intensity ratios of the AR-profiles,
4. comparison of the intensity ratios with those calculated with the FP-method.

The geometry of the instrument has also been considered to retrieve the irradiation and detection angles when only the tilting angle was known. If we consider the vector of the source $(\vec{t})$, the vector of the sample $(\vec{s})$, and the vector of the detector $\left(\vec{d}\right)$, in the coordinate system depicted in Fig. 2, we have: $\vec{t} = (0, 0, -1)$, $d\rightarrow = (1/\sqrt{2}, -1/\sqrt{2}, 0)$, and the vector of sample surface, which represent the rotation, is $\vec{s} = (sin\alpha, 0, cos\alpha)$. We can then calculate the angle of irradiation (ϕ), and the angle of detection (θ) as:

$$sin\phi = sin\left(\frac{\pi}{2} - \alpha\right) = cos\alpha \tag{5}$$

$$sin\theta = \vec{d} \cdot \vec{s} = \frac{sin\alpha}{\sqrt{2}} \tag{6}$$

Obtaining for the effective attenuation correction:

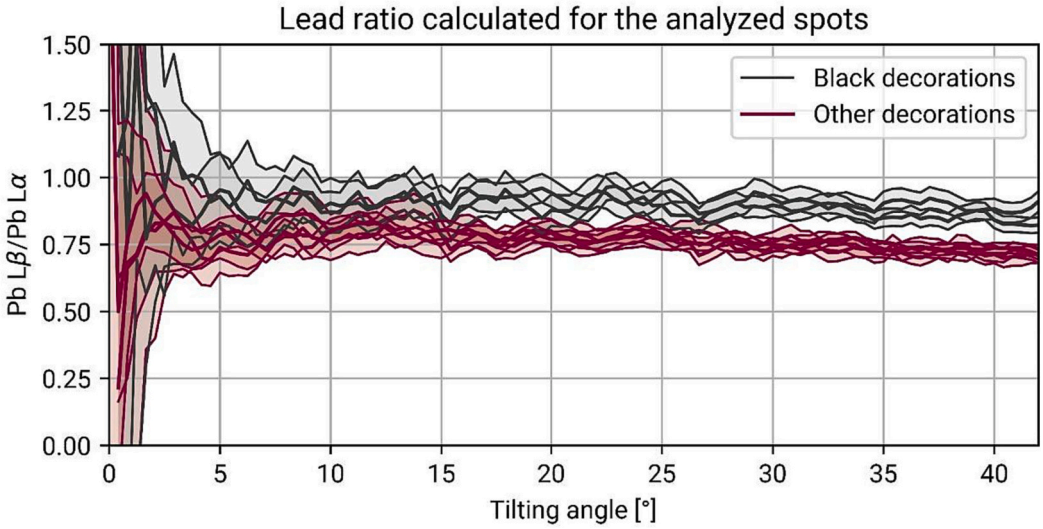

Fig. 8. Ratio between the lead L_β and L_α line intensities for the different decorations. Here is highlighted in black the ratio calculated for the black decorations and in pink the one calculated for all the other decorations (white glaze, and the dark/light blue glaze. (For interpretation of the references to color in this figure legend, the reader is referred to the web version of this article.)

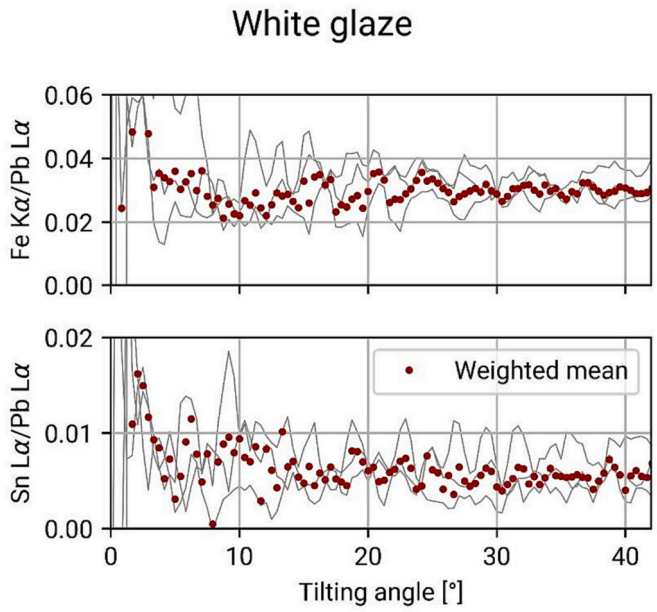

Fig. 9. Intensity ratio evaluated for iron and tin in the white glaze measurement points, for both the ratios, the reference fluorescence line is lead L_α.

$$\mu_m^*(E, E_q, \alpha) = \frac{\mu_m(E)}{cos\alpha} + \frac{\sqrt{2}\,\mu_m(E_q)}{sin\alpha} \tag{7}$$

3.4. The FP-algorithm

As a multi-layer system is complex, the calculations of the Fundamental Parameters algorithm data require significant machine time and memory. To reduce the machine time, we wrote an in-house Python code, running with the package *xraylib* [65], working in a 6-dimensional space, whose dimensions are summarized in Table 1. Before applying this algorithm for the study of this sample, we tested it on gilded laboratory-made samples where the composition of each layer is known, and we have an estimate of each layer's thickness.

The result is then a 6-dimensional matrix, in which each element represents the fluorescence intensity of one analyte, composing a specific layer, excited by one discretized energy of the source, for a tilting angle of the sample and attenuated by a top-layer with a certain thickness and composition. If this matrix is collapsed, summing along the dimensions *m* and *n* (source energies and layers), we obtain the total intensity of each element, measured with a specific geometry, and attenuated by a top layer with a defined thickness and composition. The use of multidimensional matrices has the advantage of reducing the number of cycles and the calculation time; anyway, as more data are stored in the process, more space is needed (even though the final space required is roughly the same).

To operate the code needs to know the source distribution and the detector efficiency, the former has been deconvoluted following the work of Padilla et al. [66], while the latter has been calculated using the information given by the manufacturer. The code is executed in a four steps sequence:

1. Definition of the parameters (the only part of the script which is changed by the user).
2. Entering the cycles: the index of the final data frame is created to reduce the required space and calculation time; the variables are inserted in the calculation algorithm.
3. Final definition of the structure: the structure of the sample is created, if defined as oxides composition then is converted into elemental composition; the density of each layer is then calculated using the oxides density and their concentration using eq. 8:

$$\rho^{-1} = \sum \frac{w_q}{\rho_q} \tag{8}$$

where ρ_q is the density of each oxide and $w_q$is its concentration in the layer.

4. FP-calculations: The calculations are processed. The data that are constant for all the cycles (like the probability emission of each fluorescence line) are calculated only on the first cycle to reduce the computing time; the data are finally stored

A more detailed description of the code can be found in the supplementary materials.

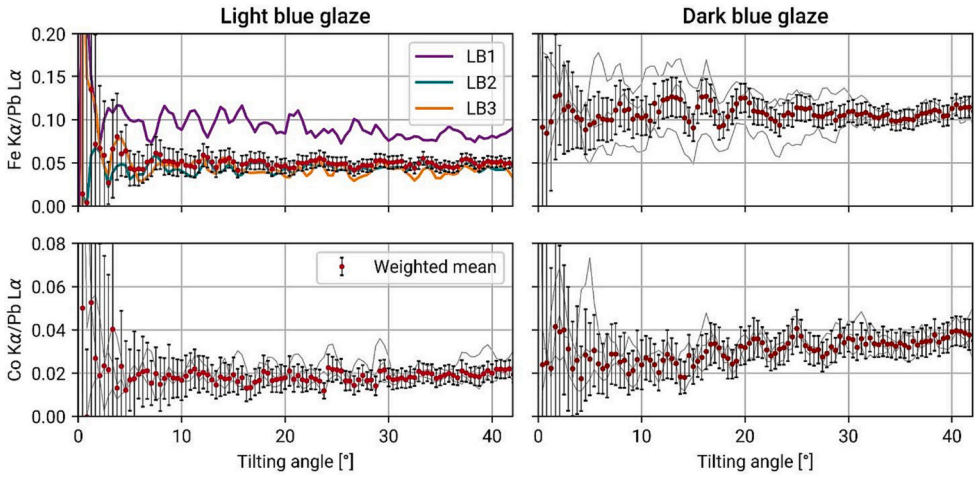

Fig. 10. Intensity ratio evaluated for cobalt and iron in the blue glaze measurement points, for both the ratios, the reference fluorescence line is lead L_α. On the top left collected from the light blue glaze, on the right those collected from the dark blue glaze. (For interpretation of the references to color in this figure legend, the reader is referred to the web version of this article.)

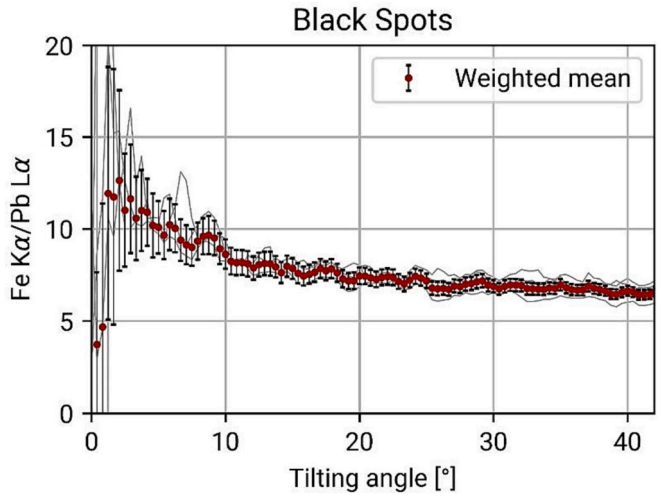

Fig. 11. Fe K_α/Pb L_α intensities weighted mean ratio for the Black spots sampling points.

4. Results and discussion

4.1. Qualitative analysis

The only information on the ceramic body composition known a priori are those reported in a previous study [58], summarized in Table 2. The white glaze is characterized by a high content of lead (26%) and the presence of tin (3.5%). For such a high content of lead, the white glaze can be considered as of infinite thickness.

The cumulative spectra were obtained by summing all the XRF spectra composing the AR-XR measurement giving an idea of the composition of the different spots, Fig. 4. The white glaze (yellow spectrum), for instance, is mainly characterized by the presence of lead and tin, whose L_α line can be distinguished between the potassium and calcium K_α lines. It also contains traces of iron, manganese, and nickel. Blue decorations (dark blue and blue spectra) contain a high amount of lead (the L_β line intensity is higher concerning that of the white glaze), cobalt as a chromophore, and arsenic, usually co-related to cobalt; and also, a higher amount of iron is attested. Cobalt and arsenic are usually difficult to quantify especially if iron and lead are present in the sample. Finally, black decorations (gray spectra) are characterized by a high content of iron (higher for the thicker spots and lower for the thinner black stripes) and a lower amount of lead with respect to the white glaze.

In the spectra collected from colored glazes, we cannot distinguish or detect the L_α fluorescence line of Sn, which is characteristic of the white glaze. As Sn-L_α is a low energy line (3.44 keV), it gives information on the superficial presence of tin; while the K_α line (which has an energy of 25.2 keV) would have given information on the in-depth presence but the amplifier settings do not allow its detection. If possible, the comparison of these two lines would have certainly given more information on the structure of the sample. Finally, at 2.35 keV is possible to see the M lines of lead, suggesting that lead is always present on the sample surface, independent of the decoration.

It is interesting to look at the raw profiles of the blue decorations, depicted in Fig. 5. We plotted here the lead profiles, which we use as a reference for our normalization, and the chromophore profiles (cobalt and iron), which are characteristic of the blue glaze. The shape of the profiles of the dark blue glaze, especially for the point DB1 and DB2, do not increase steadily, as the others. They show decrements after 32° and 37°, probably due to the tridimensional shape of the decoration. The blue glaze indeed is not flat but is thicker in the center (dark blue glaze) and thinner on the borders (light blue glaze), as observed in Fig. 1B. Thus, when analyzing the borders, the glaze can be considered flat, even though it is not parallel to the sample surface, while the dark blue areas may give shadowing effects. For this reason, the use of intensity ratio can be more effective, as geometrical effects that would influence the intensity of all the elements, in the same way, are canceled out.

Before proceeding with the ratio data analysis, we evaluated the shapes of the profile's ratios calculated for different samples with the FP-method. The ratios have been calculated for a bulk sample and a bilayer sample; in the second case, we changed different parameters to observe how they affected the ratio distribution. The monolayer sample mimicked the composition of the white glaze, composed of a high content of lead and a low content of iron. The bilayer system instead was calculated keeping in mind the possible composition of a black layer, with a higher iron content. We observed then that the Fe Kα/Pb Lα ratio calculated for a monolayer bulk sample, Fig. 6, is nearly linear, as can be seen from the values of the second derivative (dashed curves) that are close to 0 (in the order of 10^{-4}). Instead, if we observe a bilayer system (Fig. 7) we observe that both composition and thickness of the top layer highly influence the shape of the ratio profile. In the case of a top-layer rich in Fe (Fig. 7 top), the ratio Fe/Pb is high at shallow angles and decreases as the angle increases, as the influence of the bulk on the overall fluorescence signal increases; this effect is more pronounced when the top-layer is thin, as its thickness influences the probed volume in the underneath layer. If we fix the thickness and the amount of iron

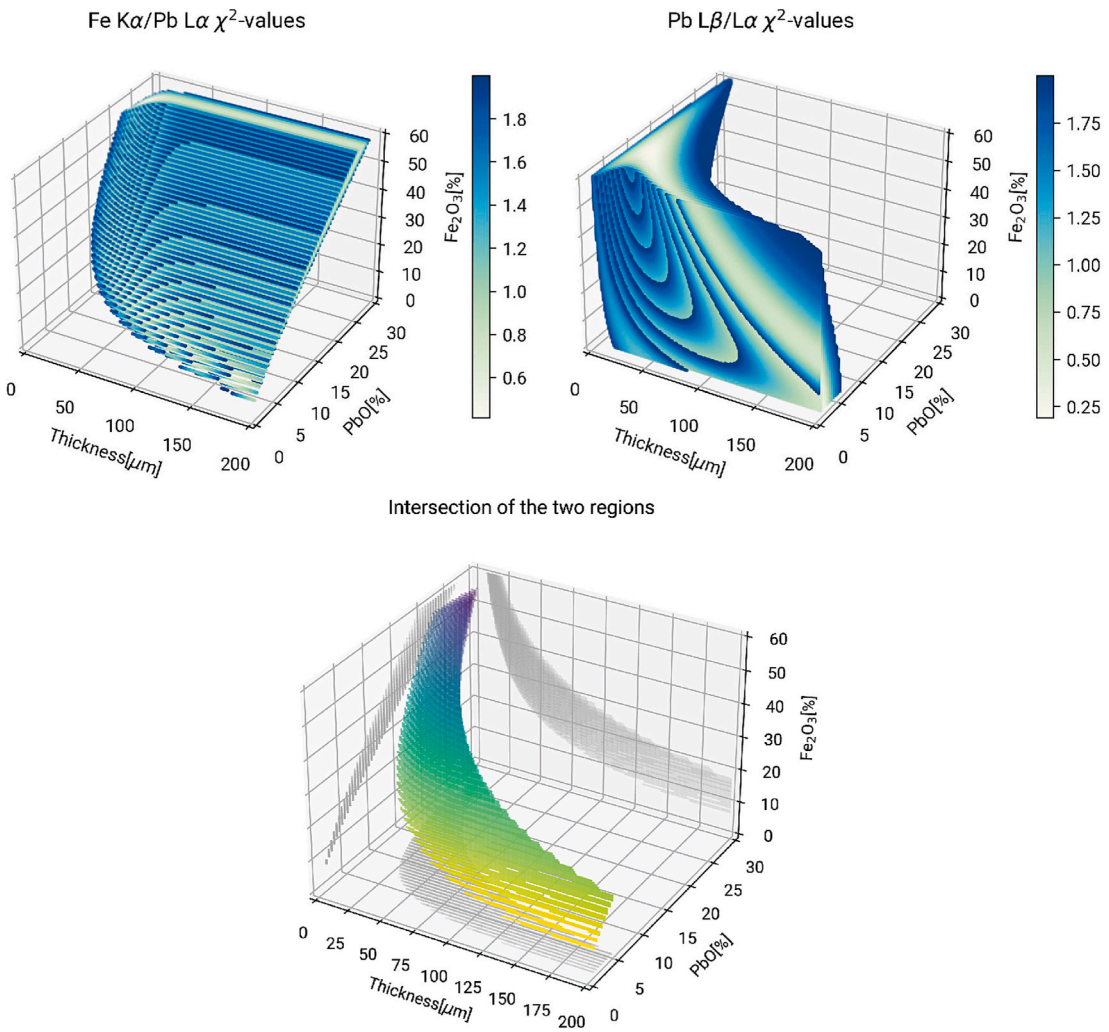

Fig. 12. Parameters for which the FP-calculations return a profile with an acceptable χ^2-value when compared with the ratio profiles. In the top-left are the points selected for having an accepted value for the Fe K_α/Pb L_α; in the top-right plot are those that have an accepted χ^2 for the Pb L_β/L_α ratio, the color represents the χ^2 value of each point. In the lower plot is the intersection of the two regions.

instead varies (Fig. 7 center) we observe that the change in shape is more pronounced for high concentrations of iron and low as the composition is very different from the composition of the bulk (26.00% of PbO and 0.76% of Fe_2O_3). Finally, for low amounts of lead, we observe an intense change in the ratio between the measures at shallow angles and steeper angles, since it is employed as a reference element (being common to the white glaze and the colored glaze all the other element intensities are normalized for lead fluorescence intensity). We can observe also that the linearity is high for very thick layers, if the iron concentration of the characteristic element is low, or if the concentration of the reference element is high (Fig. S4 in the supplementary materials).

4.2. Using the Pb L_β/L_α intensity ratio

The main element, common to all the decorations (regardless of the color) is lead, and it can then be employed as a reference element. So, it can be useful to evaluate whether the ratio of the two most intense fluorescence lines of lead (L_β/L_α) is always the same or if there is a difference (Fig. 8). If we look at the value of this profile, we can split the decorations into two groups: (I) the blue decorations and the white glaze, which present the same ratio; and (II) the black decorations which present a higher ratio. The increase of this ratio for the black decorations may be caused by the high contents of Fe causing a higher attenuation of Pb-L_α than of Pb-L_β arising from the bulk white layer.

In the case of the blue decoration, we can observe that the attenuation coefficient does not change with respect to the white glaze for the energies of the fluorescence lines of lead (10.55 keV for the L_α, and 12.62 keV for the L_β). Thus, between the white and the blue glazes, we do not expect a great difference in the matrix composition, due to the low contents of the chromophore (see the sum spectra shown in Fig. 4).

4.3. White glaze and blue decorations

If we look at the ratio calculated for the white glazes, that we consider as a reference (Fig. 9), we see that the iron/lead intensity ratios are linear, as observed for monolayer samples. We chose iron and tin as characterizing elements, because iron is the main element of the black decorations, thus a comparison may be useful, and tin characterizes the glaze opacity (Fig. 6).

For the blue decorations, we analyzed the ratios of cobalt on lead and iron on lead, because both cobalt and iron are related to the blue color of the glaze. For the dark blue glaze all the spots present similar ratios, Fig. 10, thus can be averaged out, and we can observe that the ratio is linear, remaining constant for iron (0.1), and slightly increasing for cobalt (from 0.02 to 0.04). If we look at the light blue decoration, we observe the same behavior for iron and cobalt, even if the intensity ratio is lower for both elements (iron is 0.05, and cobalt is stable at 0.02), as expected for lower contents of the coloring oxide. A note must be made

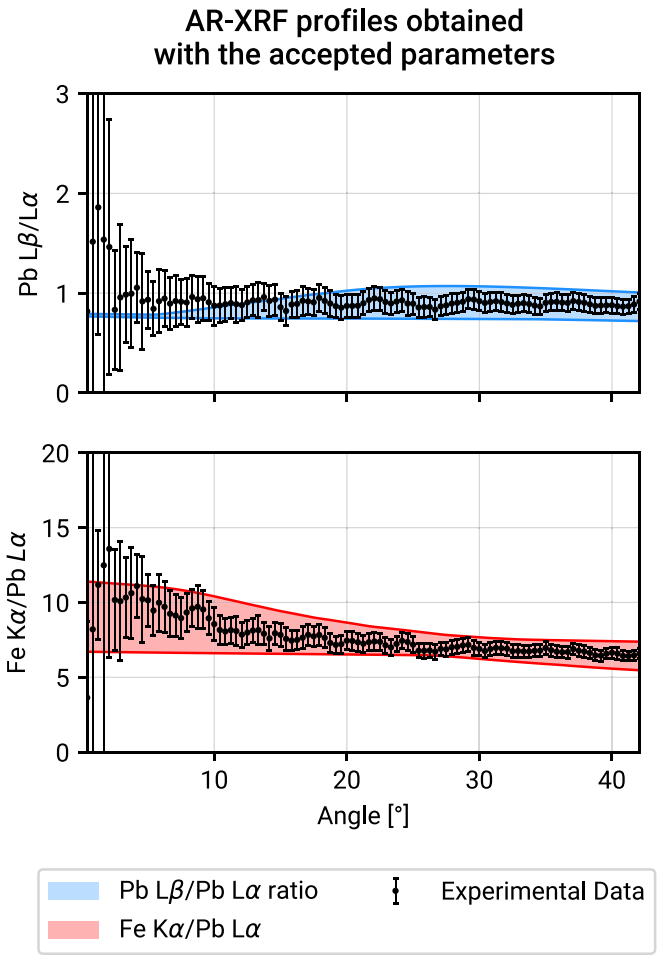

Fig. 13. Comparison of the profiles obtained with the parameters selected with the χ^2 method (blue region for the lead ratio, and red region for the iron/lead ratio) and the experimental data.

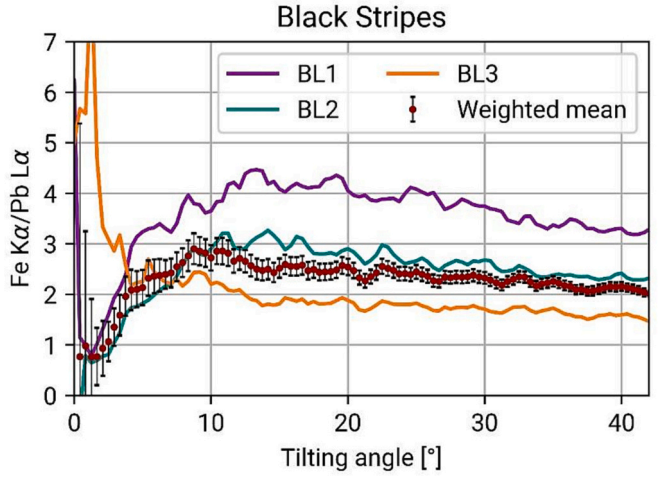

Fig. 14. Intensity ratio of the black stripe decorations.

for point LB1, collected in the light blue glaze, where the ratio of iron/lead is the same as the dark blue decoration, probability simply due to a higher content of iron.

The behavior of the ratios suggests that for XRF the blue decorations cannot be distinguished from the white glaze underneath, the possibilities are two: (I) the blue decorations (indistinctly if they are darker or

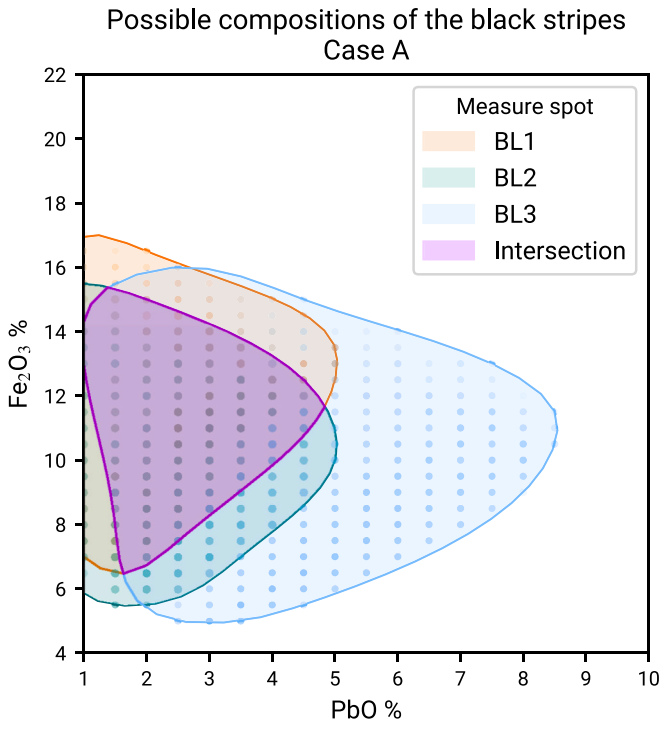

Fig. 15. Region of the composition of the three sample points taken on the black stripes, each color, shows the compositional range of one sample point; the intersection, in purple, represents the supposed composition of the black glaze for a covering layer with a lead content of 26% (Case A). (For interpretation of the references to color in this figure legend, the reader is referred to the web version of this article.)

Table 1
Dimensions employed to calculate the Fundamental Parameters profiles. The numbering follows the Python convention for which the first element is the 0 element.

Dimension	Name	Description
0	*m*	Source Energy
1	*n*	Number of layers
2	*o*	Fluorescence line
3	*p*	Angle of tilting
4	*q*	Thickness of the top layer
5	*r*	Composition of the top layer

Table 2
Composition of the white glaze in the Puebla sample already published by [58].

Glaze composition (wt%)					
Na_2O	4.3	SiO_2	54.1	Fe_2O_3	0.76
MgO	0.23	K_2O	3.08	SnO_2	3.5
Al_2O_3	9.7	CaO	1.2	PbO	26.0

Table 3
Concentration of the black glaze as calculated using AR-XRF; each range has been calculated considering a different composition of the top glaze.

Top Glaze Composition	Black glaze composition	
	PbO %	Fe_2O_3%
Case A	1.0–4.5%	7.0–15.5%
Case B	1.0–4.5%	7.0–17.5%
Case C	2.5–6.0%	7.5–16.0%

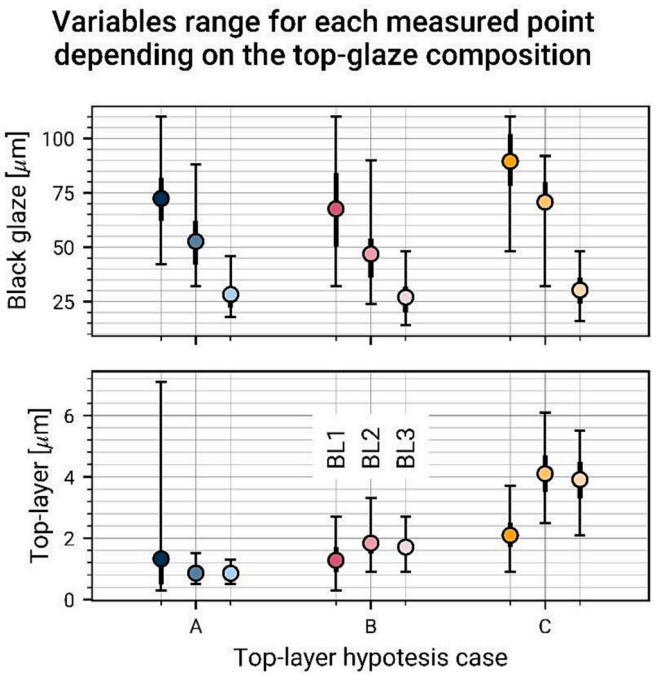

Fig. 16. Result of the thickness range calculations. Each color (blue, yellow, and pink) corresponds to a different composition of the covering top glaze; each hue, instead, represents one of the measured sample spots. The dots represent the median value for each parameter, the thick line the interquartile range, and the thin line the total range of distribution. (For interpretation of the references to color in this figure legend, the reader is referred to the web version of this article.)

lighter) are too thick for the X-rays to penetrate the white glaze, (II) the compositions of the blue and white glaze are too much alike to evaluate differences with XRF performed with this experimental setup. Indeed, also from the image collected on the fracture (see Fig. 1B), we can observe that the color change is given by the thickness of the decoration, we can expect then that the dark blue decoration is of infinite thickness for the considered energies. For the light blue decoration, we cannot exclude that we are registering a signal from the underlying white glaze. As a matter of fact, we notice that the ratio of iron and cobalt is halved, however, it has behavior similar to that observed in the dark blue glaze. This can suggest a diffusion of the blue glaze inside of the white glaze so that for thinner layers we also see a higher dilution of the chromophore elements, yet we are in a regime of infinite thickness, thus we cannot distinguish the presence of different layers.

4.4. Black spots

As can be seen in Fig. 11, the ratio of Fe K_α and Pb L_α intensities is higher for low angles, and decreases for higher angles, while the ratio of Pb L_β/L_α is higher than the one calculated for the white glaze, Fig. 8. This behavior can be easily described if we consider the presence of two different layers: the black decoration (iron-rich layer), and the white glaze, lead-rich layer. The aim now is to evaluate whether is possible to retrieve a range for the composition and thickness of the top layer. The sample points present the same ratio for both iron and lead; thus, they can be averaged out, and only the mean profile, which can be considered representative of the analyzed spot, is considered (indeed all the measured points have been collected on the same decoration).

With the FP we calculated the possible ratio for different top-layer's composition and thickness. As we will not be able to define the top-layer minor and trace elements, we assumed it to be composed only of its main elements expressed as oxides: Fe_2O_3, PbO, and SiO_2. We hypothesize that the composition can vary between a minimum value up to a maximum one, using the content of SiO_2 to close at 100%. In particular:

- Fe_2O_3 from 1 to 60% with a step of 0.5%
- PbO from 1 to 35% with a step of 0.5%

To define the thickness range, we previously calculated the infinite thickness limit for Pb L_α and Fe K_α considering the above-mentioned compositional range. Assuming that the emitted radiation is perpendicular to the sample surface and attenuated by 96%, applying the Lamber-Beer equation [Eq. 1], we estimated that the maximum path length for Pb Lα in the lightest possible matrix is 500 μm, while for the heaviest composition, it is 100 μm; for Fe Kα, it goes from 175 to 50 μm for the same conditions. Given these values, we chose a range from 0 to 200 μm (exceeding the maximum path length for iron) with a step of 1 μm.

The parameters that will fit the data have been obtained by comparing the fitted and the experimental data through the χ^2-method [67]. We considered acceptable all the compositional and thickness values that gave a profile for which the χ^2-test is less or equal to 2 (equal to the variance of the reduced χ^2 distribution) for (I) lead L_α/L_β intensities ratio and (II) the iron/lead intensities ratio. The variables that give the accepted χ^2 values for the two ratios are shown in Fig. 12.

From these plots, we can observe that the Fe/Pb ratio selects a narrow stripe in the PbO-Fe_2O_3 projection plot, while the ratio of the lead fluorescence lines divides the space into two regions, depending on the lead concentration, which must be lower than the 26%. Regarding the thickness we can observe that it can be evaluated higher than 20 μm, thus what we are observing is mainly the effect of self-attenuation on the fluorescence signal of both iron and lead. In this case, AR-XRF can only evaluate the existence of two different layers, however, no information on its thickness or composition can be extracted, except for the lead content which is equal to or lower than the one measured in the white glaze. Fig. 13 instead shows a comparison of the experimental data with the profiles generated with the parameters selected. As can be observed, the theoretical data well enclose the experimental data.

4.5. Black stripes

The black stripes decorations show different behavior with respect to the black spots, as shown in Fig. 13. Firstly, we can observe that for the Fe/Pb intensities ratio the sample points show different profiles, thus we cannot average out the results, as they will not be representative. For this very reason we chose to treat these measurements separately, comparing each measurement with the calculated data. The second feature we observe is that the iron profile is sensitively different with respect to those observed for bilayer samples, in this case the profile increases for the first 10°, then it decreases steadily. We considered the possibility of an escape of the fluorescence photon of lead emitted from the white glaze, from the border of the sample, however, the measured points are farther from the border with respect to the escape depth calculated for the published composition of this material. That is why here we supposed the presence of a tri-layer system, where there is a first layer with low iron content, a second layer with high iron content (black decoration), and then the white glaze underneath. In literature, to our knowledge, no data on a covering layer can be found, thus, with the AR-XRF technique we can only suppose that this behavior can be ascribed to an alteration of the glaze, the segregation of some elements in different volumes of the glaze, or the formation of low-iron content layer during the firing process.

As this information cannot be retrieved, for the analysis of this system we employed four variables, the composition and thickness of the black layer, described as in the black spot case, and the composition and thickness of a covering iron-poor layer. As we do not know in principle the composition of the top-covering layer, as no literature data has been found, we evaluated three possible cases:

A. The black glaze during the firing process has been covered by a thin layer of the white glaze.
B. A reaction process has left a top layer with a lead concentration between the background glaze and the silicon oxide content.
C. The black glaze during the firing process has undergone a process of segregation that has left a thin layer of silicon oxide on the surface.

The three hypotheses of the sample three-layer structure simulated can be summarized as (A) white glaze, black glaze, white glaze; (B) white glaze (with a lead oxide concentration of 10%), black glaze, white glaze; and (C) SiO_2, black glaze, and white glaze. The top layer was simulated with a thickness of 0.1-20 μm with a step of 0.2 μm; the black layer instead has been simulated with a thickness ranging from 1 to 110 μm with a step of 2 μm. The concentrations of iron and lead oxides in the black layer were changed in a range of 5 to 24% with a step of 0.5% for Fe_2O_3, and from 0 to 15% with a step of 0.5% for PbO.

Each sample point has then been compared with all the simulated data to find the best match. To reduce the number of data we also have to consider that the composition of the black stripes is the same for each sampling point (we expect indeed the potter to have employed the same material for the decorations with the same color around the sample), thus the differences in the profiles are due to the thicknesses of the black stripe or the supposed top-glaze. The black glaze decoration thus, is considered to be the intersection of the possible compositions found considering the three different measurement points, in Fig. 14; the compositional range inferred from the data analysis is instead reported in Table 3.

The compositions calculated in the three cases are quite similar to each other and show a very low content of lead in the black glaze and a content of iron between 7% and 16%. From the compositions, we can then retrieve the corresponding thicknesses, whose distributions (median value, interquartile range, and total range) are summarized in Fig. 15. Each color represents the thickness distribution for each simulated case and each point (blue: Case A, pink: case B, yellow: case C). In the upper plot, we can observe that the thickness value is not affected by the composition of the top glaze, as each measurement point has more or less the same thickness. The black glaze of BL1 is calculated to be the thickest, and its maximum value is above 110 μm, in this case, the median value may be an underestimation. Sample point BL2 shows a median thickness of nearly 50 μm, with an overall range spanning from 20 to 80 μm (in case B), while sample point BL3 seems to be the thinnest with a range between 14 and 47 μm. Finally, in the lower plot in Fig. 15, we can observe the calculated thickness for the covering glaze, whose value is generally lower than 6.1 μm, reaching the lower range for the highest content of lead (case A), which increases both the attenuation and the density. In the case of sample BL1, we see that the top-layer thickness is higher than 6 μm, however, we can observe that the interquartile range is much narrower (Fig. 16).

In this case, where different structures with the same composition have been found on the same sample, AR-XRF can be employed to retrieve information on the layer structure, however, we needed to assume unknown structural data, that cannot be retrieved with AR-XRF alone, as the presence and composition of a transparent and thin top-layer covering glaze.

To finally discriminate the three cases, we could in principle also employ the M-lines of lead, whose profile would be very sensitive to small thicknesses of the layer: for all the cases considered here, the linear attenuation coefficient at the Pb M_α fluorescence lines are quite similar: 3080 cm^{-1} for SiO_2, and 3534 cm^{-1} for the white glaze containing 26% of lead oxide. This implies an escape depth of nearly 10.5 μm in SiO_2, and 9.1 in the white glaze (case B has an intermediate value). If we observe the median thickness obtained in the case C: 2 and 4 μm, we can calculate that the silica layer would absorb 45% and 70% of the radiation of the Pb-M_α lines. However, we do not observe any change in their intensity, for that reason we exclude that the top layer is constituted of pure silica.

5. Conclusions

The analysis of layered samples using AR-XRF has already provided good results in the case of laboratory-made gilded samples [51]. In this paper, we showed the application of the same technique, coupled with FP-calculations, to describe the structure of the glaze decoration of a Puebla majolica sample, a real case that presents a much higher number of variables. The decorations on the investigated artifact can be classified into three groups: blue decoration, black spots, and black stripes, placed on top of a homogenous thick white glaze. In this case, only the composition of the white glaze was known, while the composition and thickness of the other decorations were unknown. XRF measurements have shown that the main components of the white glaze are lead and tin, employed to reduce the softening temperature and to opacify the glaze. Blue decorations show a similar composition with the addition of cobalt as chromophore and iron. Finally, black decorations, both the spots and the stripes, showed an intense signal of iron, and a lower signal of lead.

From this study we could observe that the AR-XRF technique can in some cases give information on the presence of a covering layer by observing the ratio of the fluorescence lines. For our analysis, we chose to employ the fluorescence lines of the chromophore, characteristic of the colored glazes, and the fluorescence line of lead, which is common to the colored and white glaze. However, the information retrieved depends mostly on the number of parameters and the thickness of the layer investigated. In the case of the blue glaze, AR-XRF cannot discriminate the presence of two different layers. Indeed, in this case, the colored glaze is very thick, and the composition is similar to that of the white glaze underneath, besides, a diffusion of the blue glaze inside the white glaze can also be observed in the fractures. For this reason, the blue-colored regions are described as a unique layer of infinite thickness.

For the black decorations, we could observe the presence of, at least, two layers; in this case, we tried to obtain information on the thickness and composition of the black glaze, assuming its composition was constituted only by the main components: silicon oxide, iron oxide, and lead oxide.

In the case of the black spots, the AR-XRF profiles are very similar showing the presence of a bilayer system. Moreover, we could not retrieve information on the black glaze thickness or composition, apart from the fact that the content of lead is equal to or lower than the content of lead in the white glaze. Probably, the high thickness of the black glaze may reduce the capability of the technique to obtain useful information, as in this case, variations in thickness and composition do not significantly vary the fluorescence line ratios.

Finally, for the black stripes, without any other information, we could assume the presence of a three-layer system. In this case, then, the number of variables is too high to characterize the structure. Even though we can infer that the covering glaze has a low iron content, we can only assume its composition. The three cases studied are (A) covering glaze with a composition similar to the white glaze, (B) covering glaze with a lower lead content respect with to the white glaze, and (C) covering layer of silicon oxide. We could retrieve a compositional range for the lead and iron contents and find the thickness of the black glaze in each measured point. We can observe that the thickness of the black glaze is consistent for each measured spot independently from the assumed covering layer. Finally, we observed that, if present, the covering glaze is very thin. Thanks to the evaluation of the Pb-M lines and the attenuation of the top layer in the three cases considered we could finally exclude the presence of SiO_2 in the covering glaze, as, for the thickness calculated it would attenuate >50% of their intensity.

In conclusion, the AR-XRF technique can be employed to analyze the structure of a layered sample, however alone it cannot give complete information on the composition and thickness of the different layers. Indeed, if the layers are infinitely thick, nearly infinitely thick, or diffusion phenomena are observed, any information or very few assumptions can be made. Even in the case of a thin layer, AR-XRF must be

supported by some a priori knowledge (as the composition of the bulk, or in the case of a three-layer system, the composition of one of the two layers, here assumed in three different cases), that can be obtained with other techniques.

Funding

This research did not receive any specific grant from funding agencies in the public, commercial, or not-for-profit sectors.

CRediT authorship contribution statement

Jacopo Orsilli: Conceptualization, Methodology, Software, Investigation, Formal analysis, Writing – original draft, Writing – review & editing, Visualization. **Marco Martini:** Writing – review & editing. **Anna Galli:** Conceptualization, Methodology, Validation, Writing – original draft, Writing – review & editing, Project administration, Funding acquisition.

Declaration of Competing Interest

The authors declare that they have no known competing financial interests or personal relationships that could have appeared to influence the work reported in this paper.

Data availability

The raw/processed data required to reproduce these findings cannot be shared at this time as the data also forms part of an ongoing study.

Acknowledgment

We would like to thank Alessandro Migliori and Roman Padilla Alvarez, from the Nuclear Science and Instrumentation Laboratories of the International Atomic Energy Agency (IAEA) for their priceless support during the analytical process, for hosting us in their laboratory, and for their precious insights and critics.

Appendix A. Supplementary data

Supplementary data to this article can be found online at https://doi.org/10.1016/j.sab.2023.106809.

References

[1] K. Uhlir, M. Griesser, G. Buzanich, P. Wobrauschek, C. Streli, D. Wegrzynek, A. Markowicz, E. Chinea-Cano, Applications of a new portable (micro) XRF instrument having low-Z elements determination capability in the field of works of art, X-Ray Spectrom. 37 (2008) 450–457, https://doi.org/10.1002/xrs.1074.
[2] F. Alloteau, P. Lehuédé, O. Majérus, I. Biron, A. Dervanian, T. Charpentier, D. Caurant, New insight into atmospheric alteration of alkali-lime silicate glasses, Corros. Sci. 122 (2017) 12–25, https://doi.org/10.1016/j.corsci.2017.03.025.
[3] O. Majérus, P. Lehuédé, I. Biron, F. Alloteau, S. Narayanasamy, D. Caurant, Glass alteration in atmospheric conditions: crossing perspectives from cultural heritage, glass industry, and nuclear waste management, Mater. Degrad. 4 (2020) 1–16, https://doi.org/10.1038/s41529-020-00130-9.
[4] A. Rodrigues, S. Fearn, M. Vilarigues, Historic K-rich silicate glass surface alteration: behaviour of high-silica content matrices, Corros. Sci. 145 (2018) 249–261, https://doi.org/10.1016/j.corsci.2018.10.010.
[5] E. Greiner-Wronowa, D. Zabiegaj, P. Piccardo, Glass–metal objects from archaeological excavation: corrosion study, Appl. Phys. A Mater. Sci. Process. 113 (2013) 999–1008, https://doi.org/10.1007/s00339-013-7728-x.
[6] M. Bouchar, P. Dillmann, D. Neff, New insights in the long-term atmospheric corrosion mechanisms of low alloy steel reinforcements of cultural heritage buildings, Materials. 10 (2017) 670, https://doi.org/10.3390/ma10060670.
[7] A. Negi, I.P. Sarethy, Microbial biodeterioration of cultural heritage: events, colonization, and analyses, Microb. Ecol. 78 (2019) 1014–1029, https://doi.org/10.1007/s00248-019-01366-y.
[8] M. Bethencourt, T. Fernández-Montblanc, A. Izquierdo, M.M. González-Duarte, C. Muñoz-Mas, Study of the influence of physical, chemical and biological conditions that influence the deterioration and protection of underwater cultural heritage, Sci. Total Environ. 613–614 (2018) 98–114, https://doi.org/10.1016/j.scitotenv.2017.09.007.
[9] G.M. Ingo, A.D. Bustamante, W. Alva, E. Angelini, R. Cesareo, G.E. Gigante, S.D.P. A. Zambrano, C. Riccucci, G. Di Carlo, E.I. Parisi, F. Faraldi, L. Chero, J.S. Fabian, Gold coated copper artifacts from the Royal Tombs of Sipán (Huaca Rajada, Perù): manufacturing techniques and corrosion phenomena, Appl. Phys. A Mater. Sci. Process. 113 (2013) 877–887, https://doi.org/10.1007/s00339-013-7711-6.
[10] L. Bonizzoni, A. Galli, G. Poldi, M. Milazzo, In situ non-invasive EDXRF analysis to reconstruct stratigraphy and thickness of renaissance pictorial multilayers, X-Ray Spectrom. 36 (2007) 55–61, https://doi.org/10.1002/xrs.930.
[11] M. Bertucci, L. Bonizzoni, N. Ludwig, M. Milazzo, A new model for x-ray fluorescence autoabsorption analysis of pigment layers, X-Ray Spectrom. 39 (2010) 135–141, https://doi.org/10.1002/xrs.1216.
[12] L. Bonizzoni, C. Colombo, S. Ferrati, M. Gargano, M. Greco, N. Ludwig, M. Realini, A critical analysis of the application of EDXRF spectrometry on complex stratigraphies, X-Ray Spectrom. 40 (2011) 247–253, https://doi.org/10.1002/xrs.1320.
[13] S.A. Barcellos Lins, S. Ridolfi, G.E. Gigante, R. Cesareo, M. Albini, C. Riccucci, G. di Carlo, A. Fabbri, P. Branchini, L. Tortora, Differential X-ray attenuation in MA-XRF analysis for a non-invasive determination of gilding thickness, Front. Chem. 8 (2020) 175, https://doi.org/10.3389/fchem.2020.00175.
[14] J. Bell, P. Nel, B. Stuart, Non-invasive identification of polymers in cultural heritage collections: evaluation, optimisation and application of portable FTIR (ATR and external reflectance) spectroscopy to three-dimensional polymer-based objects, Herit. Sci. 7 (2019) 95, https://doi.org/10.1186/s40494-019-0336-0.
[15] G. Barone, M.D. Bella, M.A. Mastelloni, P. Mazzoleni, S. Quartieri, S. Raneri, G. Sabatino, Pigments characterization of polychrome vases production at Lipára: new insights by noninvasive spectroscopic methods, X-Ray Spectrom. 47 (2018) 46–57, https://doi.org/10.1002/xrs.2810.
[16] M. Manfredi, E. Barberis, F. Gosetti, E. Conte, G. Gatti, C. Mattu, E. Robotti, G. Zilberstein, I. Koman, S. Zilberstein, E. Marengo, P.G. Righetti, Method for noninvasive analysis of proteins and small molecules from ancient objects, Anal. Chem. 89 (2017) 3310–3317, https://doi.org/10.1021/acs.analchem.6b03722.
[17] H. Paiva de Carvalho, S.O. Sequeira, D. Pinho, J. Trovão, R.M.F. da Costa, C. Egas, M.F. Macedo, A. Portugal, Combining an innovative non-invasive sampling method and high-throughput sequencing to characterize fungal communities on a canvas painting, Int. Biodeterior. Biodegrad. 145 (2019), 104816, https://doi.org/10.1016/j.ibiod.2019.104816.
[18] A. Galli, L. Bonizzoni, E. Sibilia, M. Martini, EDXRF analysis of metal artefacts from the grave goods of the Royal Tomb 14 of Sipán, Peru, X-Ray Spectrom. 40 (2011) 74–78, https://doi.org/10.1002/xrs.1298.
[19] L. Bonizzoni, C. Canevari, A. Galli, M. Gargano, N. Ludwig, M. Malagodi, T. Rovetta, A multidisciplinary materials characterization of a Joannes Marcus viol (16th century), Herit. Sci. 2 (2014) 15, https://doi.org/10.1186/2050-7445-2-15.
[20] A. Galli, M. Caccia, R. Alberti, L. Bonizzoni, N. Aresi, T. Frizzi, L. Bombelli, M. Gironda, M. Martini, Discovering the material palette of the artist: a p-XRF stratigraphic study of the Giotto panel 'god the father with angels': discovering the pigment palette using a p-XRF stratigraphic analysis, X-Ray Spectrom. 46 (2017) 435–441, https://doi.org/10.1002/xrs.2751.
[21] L. Bonizzoni, A. Galli, M. Gondola, M. Martini, Comparison between XRF, TXRF, and PXRF analyses for provenance classification of archaeological bricks, X-Ray Spectrom. 42 (2013) 262–267, https://doi.org/10.1002/xrs.2465.
[22] L. Bonizzoni, S. Caglio, A. Galli, G. Poldi, Comparison of three portable EDXRF spectrometers for pigment characterization, X-Ray Spectrom. 39 (2010) 233–242, https://doi.org/10.1002/xrs.1253.
[23] L. Bonizzoni, A. Galli, G. Poldi, In situ EDXRF analyses on renaissance plaquettes and indoor bronzes patina problems and provenance clues, X-ray Spectrom, Int. J. 37 (2008) 388–394, https://doi.org/10.1002/xrs.1015.
[24] C. Vanhoof, J.R. Bacon, U.E.A. Fittschen, L. Vincze, Atomic spectrometry update: review of advances in X-ray fluorescence spectrometry and its special applications, J. Anal. At. Spectrom. 37 (2022) 1761–1775, https://doi.org/10.1039/D2JA90035A.
[25] C. Vanhoof, J.R. Bacon, U.E.A. Fittschen, L. Vincze, Atomic spectrometry update – a review of advances in X-ray fluorescence spectrometry and its special applications, J. Anal. At. Spectrom. 38 (2023) (2023) 1730–1743, https://doi.org/10.1039/D3JA90026F.
[26] M. Radepont, L. Robinet, C. Bonnot-Diconne, C. Pacheco, L. Pichon, Q. Lemasson, B. Moignard, Ion beam analysis of silver leaves in gilt leather wall coverings, Talanta. 206 (2020), 120191, https://doi.org/10.1016/j.talanta.2019.120191.
[27] I. Ortega-Feliu, F.J. Ager, C. Roldán, M. Ferretti, D. Juanes, S. Scrivano, M. A. Respaldiza, L. Ferrazza, I. Traver, M.L. Grilli, Multi-technique characterization of gold electroplating on silver substrates for cultural heritage applications, Nucl. Instrum. Meth. Phys. Res. Sect. B Beam Interact. Mater. At. 406 (2017) 318–323, https://doi.org/10.1016/j.nimb.2017.02.016.
[28] F.J. Ager, M. Ferretti, M.L. Grilli, D. Juanes, I. Ortega-Feliu, M.A. Respaldiza, C. Roldán, S. Scrivano, Reconsidering the accuracy of X-ray fluorescence and ion beam based methods when used to measure the thickness of ancient gildings, Spectrochim. Acta Part B At. Spectrosc. 135 (2017) 42–47, https://doi.org/10.1016/j.sab.2017.06.017.
[29] G. Padeletti, G.M. Ingo, A. Bouquillon, S. Pages, M. Aucouturier, S. Röhrs, P. Fermo, First-time observation of Mastro Giorgio masterpieces by means of non-destructive techniques, Appl. Phys. A Mater. Sci. Process. 83 (2006) 475–483, https://doi.org/10.1007/s00339-006-3549-5.
[30] T. Pradell, A. Climent-Font, J. Molera, A. Zucchiatti, M.D. Ynsa, P. Roura, D. Crespo, Metallic and nonmetallic shine in luster: an elastic ion backscattering study, J. Appl. Phys. 101 (2007), 103518, https://doi.org/10.1063/1.2734944.

[31] P.A. Mandò, M.E. Fedi, N. Grassi, A. Migliori, Differential PIXE for investigating the layer structure of paintings, Nucl. Instrum. Meth. Phys. Res. Sect. B Beam Interact. Mater. At. 239 (2005) 71–76, https://doi.org/10.1016/j.nimb.2005.06.181.
[32] Y. Leon, Ph. Sciau, A. Bouquillon, L. Pichon, Ph. de Parseval, PIXE (particle induced X-ray emission): A non-destructive analysis method adapted to the thin decorative coatings of antique ceramics, Nucl. Instrum. Meth. Phys. Res. Sect. B Beam Interact. Mater. At. 291 (2012) 45–52, https://doi.org/10.1016/j.nimb.2012.09.010.
[33] L. Pappalardo, S. Barresi, G. Biondi, C. Caliri, F. Caruso, R. Catalano, G. Lamagna, G.A. Manenti, G. Monterosso, A. Orlando, F. Rizzo, F.P. Romano, H.C. Santos, PIXE-alpha non-destructive and in situ compositional investigation of black gloss on ancient pottery, X-Ray Spectrom. 45 (2016) 258–262, https://doi.org/10.1002/xrs.2696.
[34] A.-G. Karydas, D. Sokaras, C. Zarkadas, N. Grlj, P. Pelicon, M. Žitnik, R. Schütz, W. Malzer, B. Kanngießer, 3D Micro PIXE—a new technique for depth-resolved elemental analysis, J. Anal. At. Spectrom. 22 (2007) 1260–1265, https://doi.org/10.1039/B700851C.
[35] J.L. Campbell, W.J. Teesdale, J.A. Maxwell, Foil thickness measurement via the kb/Ka intensity ratio of proton-induced X-ray, Nucl. Instrum. Meth. Phys. Res. Sect. B Beam Interact. Mater. At. 43 (1989) 197–202, https://doi.org/10.1016/0168-583X(89)90038-4.
[36] R. Cesareo, J.T. de Assis, C. Roldán, A.D. Bustamante, A. Brunetti, N. Schiavon, Multilayered samples reconstructed by measuring Kα/Kβ or Lα/Lβ X-ray intensity ratios by EDXRF, Nucl. Instrum. Meth. Phys. Res. Sect. B Beam Interact. Mater. At. 312 (2013) 15–22, https://doi.org/10.1016/j.nimb.2013.06.019.
[37] M. Karimi, N. Amiri, A.A., Tabbakh Shabani, thickness measurement of coated Ni on brass plate using Kα/Kβ ratio by XRF spectrometry, X-Ray Spectrom. 38 (2009) 234–238, https://doi.org/10.1002/xrs.1146.
[38] J. Brocchieri, E. Scialla, C. Sabbarese, Estimation of ag coating thickness by different methods using a handheld XRF instrument, Nucl. Instrum. Meth. Phys. Res. Sect. B Beam Interact. Mater. At. 486 (2021) 73–84, https://doi.org/10.1016/j.nimb.2020.11.006.
[39] C. Bottaini, J. Mirão, A. Candeias, H. Catarino, R.J. Silva, A. Brunetti, Elemental characterisation of a collection of metallic oil lamps from South-Western al-Andalus using EDXRF and Monte Carlo simulation⋆, Eur. Phys. J. Plus. 134 (2019) 365, https://doi.org/10.1140/epjp/i2019-12894-4.
[40] T. Trojek, D. Wegrzynek, X-ray fluorescence Kα/Kβ ratios for a layered specimen: comparison of measurements and Monte Carlo calculations with the MCNPX code, Nucl. Instrum. Methods Phys. Res. Sect. Accel. Spectrometers Detect. Assoc. Equip. 619 (2010) 311–315, https://doi.org/10.1016/j.nima.2009.10.157.
[41] T. Trojek, Iterative Monte Carlo procedure for quantitative X-ray fluorescence analysis of copper alloys with a covering layer, Radiat. Phys. Chem. 167 (2020), 108294, https://doi.org/10.1016/j.radphyschem.2019.04.044.
[42] C. Bottaini, J. Mirão, M. Figuereido, A. Candeias, A. Brunetti, N. Schiavon, Energy dispersive X-ray fluorescence spectroscopy/Monte Carlo simulation approach for the non-destructive analysis of corrosion patina-bearing alloys in archaeological bronzes: the case of the bowl from the Fareleira 3 site (Vidigueira, South Portugal), Spectrochim. Acta Part B At. Spectrosc. 103–104 (2015) 9–13, https://doi.org/10.1016/j.sab.2014.10.015.
[43] K. Nakano, K. Tsuji, Nondestructive elemental depth profiling of Japanese lacquerware 'Tamamushi-nuri' by confocal 3D-XRF analysis in comparison with micro GE-XRF, X-Ray Spectrom. 38 (2009) 446–450, https://doi.org/10.1002/xrs.1163.
[44] Ž. Šmit, K. Janssens, K. Proost, I. Langus, Confocal μ-XRF depth analysis of paint layers, Nucl. Instrum. Meth. Phys. Res. Sect. B Beam Interact. Mater. At. 219–220 (2004) 35–40, https://doi.org/10.1016/j.nimb.2004.01.024.
[45] T. Trojek, R. Prokeš, R. Šefců, H. Bilavčíková, T. Čechák, Confocal X-ray fluorescence spectrometer for in-situ analyses of paintings, Radiat. Phys. Chem. 137 (2017) 238–242, https://doi.org/10.1016/j.radphyschem.2016.02.031.
[46] K. Uhlir, R. Padilla-Alvarez, A. Migliori, A.G. Karydas, I. Božičević Mihalić, M. Jakšić, I. Zamboni, R. Lehmann, M. Stelter, M. Griesser, N. Schindel, M. Alram, The mystery of mercury-layers on ancient coins — A multianalytical study on the Sasanian coins under the reign of Khusro II, Microchem. J. 125 (2016) 159–169, https://doi.org/10.1016/j.microc.2015.10.024.
[47] B. Kanngießer, W. Malzer, I. Mantouvalou, D. Sokaras, A.G. Karydas, A deep view in cultural heritage—confocal micro X-ray spectroscopy for depth resolved elemental analysis, Appl. Phys. A Mater. Sci. Process. 106 (2012) 325–338, https://doi.org/10.1007/s00339-011-6698-0.
[48] L.J. Bauer, R. Gnewkow, F. Förste, D. Grötzsch, S. Bjeoumikhova, B. Kanngießer, I. Mantouvalou, Increasing the sensitivity of micro X-ray fluorescence spectroscopy through an optimized adaptation of polycapillary lenses to a liquid metal jet source, J. Anal. At. Spectrom. 36 (2021) 2519–2527, https://doi.org/10.1039/D1JA00295C.
[49] T. Lachmann, G. van der Snickt, M. Haschke, I. Mantouvalou, Combined 1D, 2D and 3D micro-XRF techniques for the analysis of illuminated manuscripts, J. Anal. At. Spectrom. 31 (2016) 1989–1997, https://doi.org/10.1039/C6JA00220J.
[50] S. Choudhury, D.N. Agyeman-Budu, A.R. Woll, T. Swanston, T.L. Varney, D.M. L. Cooper, E. Hallin, G.N. George, I.J. Pickering, I. Coulthard, Superior spatial resolution in confocal X-ray techniques using collimating channel array optics: elemental mapping and speciation in archaeological human bone, J. Anal. At. Spectrom. 32 (2017) 527–537, https://doi.org/10.1039/C6JA00297H.
[51] P. Hönicke, Y. Kayser, B. Beckhoff, M. Müller, J.C.L. Dousse, J. Hoszowska, S. H. Nowak, Characterization of ultra-shallow aluminum implants in silicon by grazing incidence and grazing emission X-ray fluorescence spectroscopy, J. Anal. At. Spectrom. 27 (2012) 1432, https://doi.org/10.1039/c2ja10385k.
[52] V. Szwedowski, J. Baumann, I. Mantouvalou, L. Bauer, W. Malzer, B. Kanngießer, Scan-free grazing emission XRF measurements in the laboratory using a CCD, Phys. Status Solidi C 14 (2017) 1700158, https://doi.org/10.1002/pssc.201700158.
[53] J. Szlachetko, D. Banaś, A. Kubala-Kukuś, M. Pajek, W. Cao, J.C.L. Dousse, J. Hoszowska, Y. Kayser, M. Szlachetko, M. Kavčič, M. Salome, J. Susini, Application of the high-resolution grazing-emission x-ray fluorescence method for impurities control in semiconductor nanotechnology, J. Appl. Phys. 105 (2009), 086101, https://doi.org/10.1063/1.3086658.
[54] J. Baumann, Y. Kayser, B. Kanngießer, Grazing emission X-ray fluorescence: novel concepts and applications for Nano-analytics, Phys. Status Solidi B 258 (2021) 2000471, https://doi.org/10.1002/pssb.202000471.
[55] J. Baumann, D. Grötzsch, O. Scharf, T. Kodalle, R. Bergmann, F. Bilchenko, I. Mantouvalou, B. Kanngießer, A compact and efficient angle-resolved X-ray fluorescence spectrometer for elemental depth profiling, Spectrochim. Acta Part B At. Spectrosc. 181 (2021), 106216, https://doi.org/10.1016/j.sab.2021.106216.
[56] C. Fiorini, A. Gianoncelli, A. Longoni, F. Zaraga, Determination of the thickness of coatings by means of a new XRF spectrometer, X-Ray Spectrom. 31 (2002) 92–99, https://doi.org/10.1002/xrs.550.
[57] J. Orsilli, A. Migliori, R. Padilla-Alvarez, M. Martini, A. Galli, AR-XRF measurements and data treatment for the evaluation of gilding samples of cultural heritage, J. Anal. At. Spectrom. 38 (2023) 174–185, https://doi.org/10.1039/D2JA00227B.
[58] R. Padilla, O. Schalm, K. Janssens, R. Arrazcaeta, P. Van Espen, Microanalytical characterization of surface decoration in majolica pottery, Anal. Chim. Acta 535 (2005) 201–211, https://doi.org/10.1016/j.aca.2004.11.082.
[59] R. Tertian, F. Claisse, Principles of Quantitative X-Ray Fluorescence Analysis, Heyden, 1982.
[60] J.G. Iñañez, M. Madrid-Fernández, J. Molera, R.J. Speakman, T. Pradell, Potters and pigments: preliminary technological assessment of pigment recipes of American majolica by synchrotron radiation micro-X-ray diffraction (Sr-$\mu $XRD), J. Archaeol. Sci. 40 (2013) 1408–1415, https://doi.org/10.1016/j.jas.2012.09.015.
[61] R. Padilla Alvarez, R. Arrazcaeta Delgado, C. Oliva, R. Bishop, J. Blackmann, O. Schalm, Consideraciones adicionales a la clasificación de cerámica colonial en antrosoles habaneros, Bol. Gab. Arqueol. 4 (2005) 14–28.
[62] G. Roisine, N. Capobianco, D. Caurant, G. Wallez, A. Bouquillon, O. Majérus, L. Cormier, S. Gilette, A. Gerbier, The art of Bernard Palissy (1510–1590): influence of firing conditions on the microstructure of iron-coloured high-lead glazes, Appl. Phys. A Mater. Sci. Process. 123 (2017) 501, https://doi.org/10.1007/s00339-017-1089-9.
[63] D. Wegrzynek, A. Markowicz, S. Bamford, E. Chinea-Cano, M. Bogovac, Micro-beam X-ray fluorescence and absorption imaging techniques at the IAEA Laboratories, Nucl. Instrum. Meth. Phys. Res. Sect. B Beam Interact. Mater. At. 231 (2005) 176–182, https://doi.org/10.1016/j.nimb.2005.01.053.
[64] V.A. Solé, E. Papillon, M. Cotte, P. Walter, J. Susini, A multiplatform code for the analysis of energy-dispersive X-ray fluorescence spectra, Spectrochim. Acta B 62 (2007) 63–68, https://doi.org/10.1016/j.sab.2006.12.002.
[65] T. Schoonjans, A. Brunetti, B. Golosio, M. Sanchez del Rio, V.A. Solé, C. Ferrero, L. Vincze, The xraylib library for X-ray–matter interactions. Recent developments, Spectrochim. Acta Part B At. Spectrosc. 66 (2011) 776–784, https://doi.org/10.1016/j.sab.2011.09.011.
[66] R. Padilla, P. Van Espen, A. Abrahantes, K. Janssens, Semiempirical approach for standardless calibration in μ-XRF spectrometry using capillary lenses: Standardless calibration in μ-XRF using capillary lenses, X-Ray Spectrom. 34 (2005) 19–27, https://doi.org/10.1002/xrs.781.
[67] W.G. Cochran, The χ2 test of goodness of fit, Ann. Math. Stat. 23 (1952) 315–345, https://doi.org/10.1214/aoms/1177729380.